

DRIVING DISK WINDS AND HEATING UP HOT CORONAE BY MRI TURBULENCE

YUKI IO (井尾勇き)^{1,2} & TAKERU K. SUZUKI (すず木建)¹*Draft version May 2, 2019*

ABSTRACT

We investigate the formation of hot coronae and vertical outflows in accretion disks by magnetorotational turbulence. We perform local three-dimensional (3D) MHD simulations with the vertical stratification by explicitly solving an energy equation with various effective ratios of specific heats, γ . Initially imposed weak vertical magnetic fields are effectively amplified by magnetorotational instability (MRI) and winding due to the differential rotation. In the isothermal case ($\gamma = 1$), the disk winds are mainly driven by the Poynting flux associated with the MHD turbulence and show quasi-periodic intermittency. On the other hand, in the non-isothermal cases with $\gamma \geq 1.1$, the regions above 1-2 scale heights from the midplane are effectively heated up to form coronae with the temperature of ~ 50 times of the initial value, which are connected to the cooler midplane region through the pressure-balanced transition regions. As a result, the disk winds are mainly driven by the gas pressure with exhibiting more time-steady nature, although the nondimensional time-averaged mass loss rates are similar to that of the isothermal case. Sound-like waves are confined in the cool midplane region in these cases, and the amplitude of the density fluctuations is larger than that of the isothermal case.

Subject headings: accretion, accretion disks — MHD — stars: winds, outflows — planetary systems: protoplanetary disks — turbulence

1. INTRODUCTION

In accretion disks magnetohydrodynamical (MHD) turbulence is believed to work as effective viscosity and play an essential role in the outward transport of the angular momentum and the radial motion of the gas (e.g. Lynden-Bell & Pringle 1974; Balbus & Hawley 1998). Magnetorotational instability (MRI hereafter Velikhov 1959; Chandrasekhar 1960; Balbus & Hawley 1991) is a promising source of such turbulent viscosities in accretion disks.

Properties of the MRI in accretion disks have been widely studied. MHD simulations in the local shearing coordinate (Goldreich & Lynden-Bell 1965) have been extensively and intensively performed without vertical density stratification (e.g., Hawley et al. 1995; Matsumoto & Tajima 1995; Sano et al. 2004), and with the vertical stratification due to the gravity by a central object (e.g., Stone et al. 1996; Miller & Stone 2000; Davis et al. 2010; Shi et al. 2010; Okuzumi & Hirose 2011; Sai et al. 2013).

Accretion disks threaded with global magnetic fields are supposed to drive disk winds, which was first suggested by Blandford & Payne (1982) as an origin of jets from black hole accretion disks. This picture of magnetocentrally driven disk winds was extended to protostellar jets (Pudritz & Norman 1983). Outflows and jets from various types of accretion disks have been observed, e.g., from young stars (Ohashi et al. 1997; Coffey et al. 2004), and from active galactic nuclei (Tombesi et al. 2010).

These two pictures – MRI-driven turbulence in accretion disks and magnetically driven winds from disk sur-

faces involving coherent field lines – are supposed to have a close link. For instance, turbulence in disks could drive the vertical motions of the gas by the MHD turbulent pressure. Based on these considerations, Suzuki & Inutsuka (2009) and suz10 recently proposed the onset of vertical outflows from MRI-turbulent accretion disks. They performed MHD simulations in local shearing boxes with the vertical stratification and net vertical magnetic fields by taking a special care of the outgoing boundary conditions (Suzuki & Inutsuka 2006) at the vertical surfaces of the simulation boxes. They found that the disk winds are driven from the upper and lower boundaries by the Poynting flux associated with the MHD turbulence. This process can contribute to the mass loading to the basal regions of the global disk winds introduced above. Such vertical outflows are also observed in 3D global simulations (Flock et al. 2011; Suzuki & Inutsuka 2013).

Later on, such MRI-turbulent driven disk winds have been further studied from various aspects. Bai & Stone (2013) examined properties of the disk winds with stronger net vertical magnetic fields. The connection between the upflows in local simulations and the global disk winds/jets is investigated (Lesur et al. 2013; Bai & Stone 2013). Fromang et al. (2013, see also Suzuki & Inutsuka 2010) pointed out the mass fluxes of the disk winds depend on the simulation box sizes, which shows that we need great cares to handle disk winds by local shearing boxes.

Although there are limitations in the shearing box approximation, it is still useful technic to study the basic properties of MRI-turbulent driven vertical outflows. Most of previous simulations adopt an isothermal equation of state to mainly focus on the dynamics of the disk winds, apart from some works by Hirose and the collaborators who considered detailed heating and cooling processes for black hole accretion disks (Hirose et al. 2006) and protoplanetary disks (Hirose & Turner 2011). So far

stakeru@nagoya-u.jp

¹ Department of Physics, Nagoya University, Furo-cho, Chikusa-ku, Nagoya, Aichi 464-8602, Japan² Nihon Unisys, Ltd., Toyosu, Koto-ku, Tokyo, 135-8560, Japan

there has been no systematic studies done for the MRI-turbulent driven winds with different ratios of specific heats, γ even within a framework of the shearing box approximation, which is the main focus of the present paper.

2. SIMULATION SETUPS

In Suzuki & Inutsuka (2009) & Suzuki et al. (2010) we performed 3D MHD simulations in local stratified shearing boxes (Stone et al. 1996) by solving the ideal MHD equations with an isothermal equation of state. In this paper, we extend these works by explicitly solving an energy equation in a Lagrangian form,

$$\rho \frac{d}{dt} \left[e + \frac{v^2}{2} + \frac{B^2}{8\pi\rho} + \frac{\Omega^2}{2}(z^2 - 3x^2) \right] = \nabla \cdot \left[- \left(p + \frac{B^2}{8\pi} \right) \mathbf{v} + \frac{\mathbf{B}}{4\pi} (\mathbf{B} \cdot \mathbf{v}) \right], \quad (1)$$

where Ω is the Keplerian rotation frequency, e is the specific energy per mass which is related to the gas pressure, p , the density, ρ , and the effective ratio of specific heats, γ , as

$$e = \frac{1}{\gamma - 1} \frac{p}{\rho}, \quad (2)$$

and the other variables in Equation (1) have the conventional meanings. The terms involving Ω^2 in Equation (1) originate from the central object; $\Omega^2 z^2/2$ is the potential due to the vertical component of the gravity and $-3\Omega^2 x^2/2$ denotes the tidal potential.

In the energy equation above we do not explicitly consider external cooling and heating processes, *e.g.*, radiation cooling/heating, thermal conduction, and *etc.* Instead, we study their effect phenomenologically by assuming different but spatially uniform γ from 1 to 5/3 in difference cases. In our simulations, the gas is heated up mainly by the dissipation of magnetic energy, which we discuss later in this section. Taking $\gamma = 1$ (isothermal condition) indicates that we (implicitly) assume that the temperature is kept constant by an unspecified cooling that can balance the magnetic heating. On the other hand, larger γ corresponds to suppressing cooling; $\gamma = 7/5$ and $5/3$ correspond to the adiabatic conditions for diatomic and monoatomic gases, respectively.

Apart from explicitly solving the energy equation, we basically follow Suzuki & Inutsuka (2009) when performing the numerical simulations. We adopt a second-order Godunov-CMoCCT scheme (Sano et al. 1999), in which we solve the nonlinear Riemann problems with the magnetic pressure at the cell boundaries for the compressive waves and adopt the consistent method of characteristics (CMoC) for the evolution of magnetic fields (Clarke 1996). At the z boundaries, we prescribe the outgoing boundary condition by using the seven MHD characteristics (Suzuki & Inutsuka 2006).

We fix the ratio of the box sizes of the x , y , and z axes to 1:4:8, which are respectively resolved by 32, 64, and 256 spatially uniform grids. Each cell is elongated in the y direction with Δy being twice as large as Δx and Δz . The lengths in the simulations are normalized

by the initial pressure scale heights, H_0 , as

$$H_0 = \frac{\sqrt{2}c_{s,0}}{\Omega} \equiv \frac{\sqrt{2T_0}}{\Omega}, \quad (3)$$

where $c_{s,0}$ is the initial sound speed, and we also use the initial temperature, T_0 , which has the dimension of v^2 . In this paper, c_s stands for an “isothermal” sound speed, $= \sqrt{p/\rho} = \sqrt{T}$; the usual sound speed, $\sqrt{(\partial p/\partial \rho)_s} = \sqrt{\gamma p/\rho} = \sqrt{\gamma T}$, is expressed as $\sqrt{\gamma}c_s$. We initially set up the hydrostatic density structure with the constant temperature, $T = T_0$,

$$\rho = \max \left(\rho_{\text{mid},0} \exp \left(-\frac{z^2}{H_0^2} \right), 10^{-9} \rho_{\text{mid},0} \right), \quad (4)$$

where $\rho_{\text{mid},0}$ is the initial density at the midplane. In order to perform the simulations stably, we adopt a floor value, $\rho_{\text{fl}} = 10^{-9} \rho_{\text{mid},0}$ throughout the simulations. In the nonisothermal cases, the simulation boxes are larger than that of the isothermal case to treat the extended coronae as shown later. In the cases with $\gamma \geq 1.03$, the initial densities near the surface regions, $|z| > 4.55H_0$, are smaller than ρ_{fl} , hence ρ_{fl} is used for these regions. In the simulations, we use the unit of $\Omega = 1$, $H_0 = 1$, and $\rho_{\text{mid},0} = 1$; accordingly, $T_0 = 1/2$ and $c_{s,0} = 1/\sqrt{2}$. We initially impose the weak net vertical magnetic field, $B_{z,0}$, with the plasma β value, $8\pi\rho_{\text{mid},0}/B_{z,0}^2 = 10^6$ at the midplane. We start the simulations with giving small random perturbations with 0.5% of $c_{s,0}$ as seeds of the MRI. The simulations are kept running until 200 rotations ($t\Omega/2\pi = 200$).

In the simulations with $\gamma > 1$, the gas is heated by the dissipation of the magnetic energy, where the heating is done by the numerical effect in the sub-grid scale since we do not explicitly take into account resistivity. As a disk is heated up, the sound speed increases, and accordingly the pressure scale height also increases. Therefore, to study the vertical structure, the z coordinate in units of the scale height,

$$\int_0^z \frac{dz}{\langle h(z) \rangle_{x,y}} \equiv \int_0^z \frac{dz\Omega}{\sqrt{2}\langle c_s \rangle_{x,y}(z)}, \quad (5)$$

is a key quantity, where the subscripts, x, y , of $\langle \rangle$ indicate the average over a horizontal ($x - y$) plane. While $\int_0^z \frac{dz}{\langle h(z) \rangle_{x,y}} = z/H_0$ for the isothermal situation, generally $|\int_0^z \frac{dz}{\langle h(z) \rangle_{x,y}}| < |z/H_0|$ as a result of the heating for $\gamma > 1$.

The mass flux of the disk winds depends on the vertical box size in units of the scale height (Suzuki et al. 2010; Fromang et al. 2013). In order to compare the properties of the disk winds with different γ , it is desirable to adopt the same vertical box size in units of the final scale height after the steady-state conditions are achieved,

$$\int_{z_{\text{bot}}}^{z_{\text{top}}} \frac{dz}{\langle h(z) \rangle_{\Delta t_{\text{ave}}, x, y}}, \quad (6)$$

where z_{bot} and z_{top} indicate the locations of the bottom and top boundaries of the simulation box, and we take the average over Δt_{ave} (Table 1) after the magnetic fields are amplified to the saturated states, which we describe later in this section. We cannot estimate $h(z)$ in advance,

γ	$(X/H_0, Y/H_0, Z/H_0)$	$\int_{z_{\text{bot}}}^{z_{\text{top}}} dz/h(z)$	$\Delta t_{\text{ave}}(\text{rotation})$
1.0	0.9, 3.6, 7.2	7.2	140–200
1.01	1.0, 4.0, 8.0	7.1	120–200
1.03	1.35, 5.4, 10.8	7.1	100–200
1.1	4.0, 16.0, 32.0	7.3	150–200
1.2	4.0, 16.0, 32.0	7.1	130–200
1.3	4.0, 16.0, 32.0	7.3	130–200
1.4	4.0, 16.0, 32.0	7.4	120–200
5/3	4.0, 16.0, 32.0	7.2	120–200

TABLE 1

THE INITIAL BOX SIZES (2nd column) AND THE FINAL VERTICAL BOX SIZES MEASURED IN THE FINAL SCALE HEIGHTS (3rd column) AVERAGED OVER Δt_{ave} OF CASES WITH DIFFERENT EFFECTIVE RATIOS OF SPECIFIC HEATS, γ . X , Y , AND $Z(=z_{\text{top}} - z_{\text{bot}})$ IN THE 2ND COLUMN ARE THE SIZES OF x , y , AND z COMPONENTS OF THE SIMULATION BOXES.

hence we perform simulations with different box sizes and pick up one that gives the desirable value for each γ . For the isothermal case ($\gamma = 1$), we fix the vertical box size ($z_{\text{top}} - z_{\text{bot}} = 7.2H_0$, indicating $0.9H_0$ and $3.6H_0$ for the box sized in the x and y directions. For the other cases with $\gamma > 1$, we tune the initial box sizes to give the final vertical box sizes after the saturations in a range of $7.1 < \int_{z_{\text{bot}}}^{z_{\text{top}}} dz/\langle h(z) \rangle_{\Delta t_{\text{ave}}, x, y} < 7.4$.

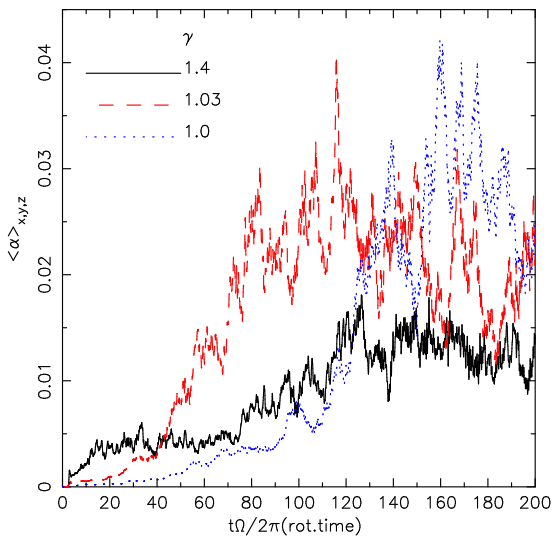


FIG. 1.— Evolution of the box-averaged $\langle \alpha \rangle_{x,y,z}$ of the three cases with $\gamma = 1.4$ (black solid), 1.03 (red dashed), and 1.0 (blue dotted). The vertical axis, $t\Omega/2\pi$, indicates time in units of one rotation.

In order to check the saturations of the magnetic fields, we monitor the box-averaged α values (Shakura & Sunyaev 1973), which is the sum of the Reynolds and Maxwell stresses normalized by the gas pressure,

$$\langle \alpha \rangle_{x,y,z} = \frac{\int_{z_{\text{bot}}}^{z_{\text{top}}} dz \langle \rho v_x \delta v_y - B_x B_y / 4\pi \rangle_{x,y}}{\int_{z_{\text{bot}}}^{z_{\text{top}}} dz \langle p \rangle_{x,y}}, \quad (7)$$

where $\delta v_y = v_y - v_{y,0}$ is the difference of toroidal velocity from the Keplerian shear flow, $v_{y,0} = -\frac{3}{2}\Omega x$. In Figure 1 we show the results of the cases with $\gamma = 1.4$ (black solid line), 1.03 (red dashed line), and 1.0 (blue dotted line). In the case with $\gamma = 1.4$, the $\langle \alpha \rangle_{x,y,z}$ appears to saturate after $t\Omega/2\pi \gtrsim 120$, and we use $\Delta t_{\text{ave}} = 120 - 200$

rotations (1 rotation = $2\pi/\Omega$) to estimate the vertical box size in the final scale height (Equation 6). Although in the case with $\gamma = 1.03$, $\langle \alpha \rangle_{x,y,z}$ almost saturates after $t\Omega/2\pi \gtrsim 80$, we use a more conservative value, $\Delta t_{\text{ave}} = 100 - 200$, because we observe that the magnetic fields near the midplane are still growing in $t\Omega/2\pi \lesssim 100$. In the isothermal case ($\gamma = 1.0$), we use $\Delta t_{\text{ave}} = 140 - 200$ rotations, because $\langle \alpha \rangle_{x,y,z}$ becomes saturated later than in the other two cases.

The initial and final box sizes and Δt_{ave} 's are summarized in Table 1. For the cases with $\gamma \geq 1.1$, the vertical box size measured in the final scale height shrinks more than a factor of 4 because of the heating, which we examine in §3. The derived Δt_{ave} is also used to examine the time-averaged vertical structures of each case in §3.

The horizontal box sizes measured in the scale height of the nonisothermal cases vary with height because of the variation of the temperature. Because the temperature is higher near the surfaces as shown later, the horizontal box sizes in units of the final scale height, $\int_{x_{\text{min}}}^{x_{\text{max}}} dx / \langle h(z) \rangle_{\Delta t_{\text{ave}}, x, y} < 0.9$ and $\int_{y_{\text{min}}}^{y_{\text{max}}} dy / \langle h(z) \rangle_{\Delta t_{\text{ave}}, x, y} < 3.6$, are smaller in the surface regions. of the nonisothermal cases. Although these horizontal sizes are insufficient to quantitatively discuss the saturations of the magnetic fields (e.g., Guan et al. 2009), we anticipate that it is still meaningful to compare the vertical disk structures with different γ .

3. RESULTS

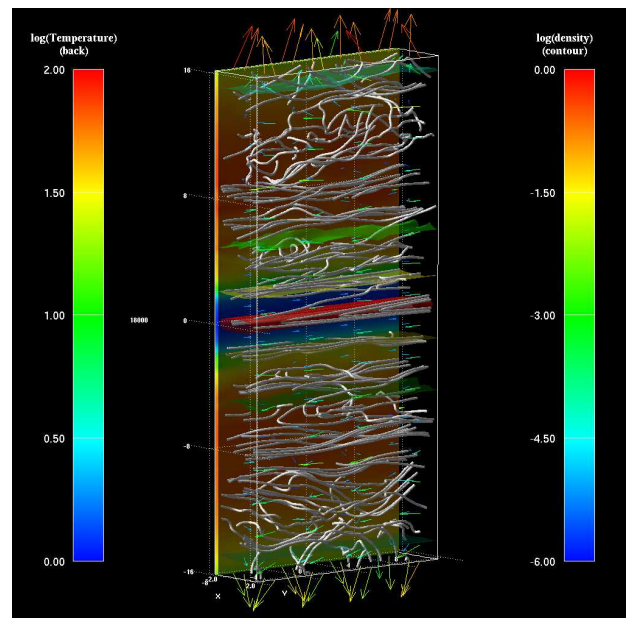


FIG. 2.— Snapshot of the simulation with $\gamma = 1.4$ at 180 rotation time ($t\Omega/2\pi = 180$). The white lines indicate magnetic field lines, the colors on the back show normalized temperature, T/T_0 , (left legend), the color contours denote iso-density surfaces (right legend), and the arrows indicate velocity fields.

Continued from the previous section we examine the time evolutions of the box averaged $\langle \alpha \rangle_{x,y,z}$ in Figure 1. After the quasi-steady saturated states are achieved, the three cases show different behaviors. The isothermal case ($\gamma = 1.0$) show large fluctuations of $\langle \alpha \rangle_{x,y,z}$ from 0.015 to 0.04. On the other hand, the case with $\gamma = 1.4$

exhibits a much milder behavior with $\langle\alpha\rangle_{x,y,z}$ kept in a range of 0.01-0.015. The case with $\gamma = 1.03$ shows an intermediate behavior; although the increase of the α is faster with showing large fluctuations in the earlier time, $2\pi t/\Omega \lesssim 120$, it settles down to a softer state later, between those for $\gamma = 1.4$ and 1.0. Interestingly enough, the similar trends are observed in the disk winds, which we discuss the details in §3.2.

Figure 2 exhibits a snapshot structure of the case with $\gamma = 1.4$ at 180 rotation time ($t\Omega/2\pi = 180$). The temperature contour on the back shows that the temperatures in $4 \lesssim |z/H_0| \lesssim 12$ increase up to more than 50 times of the initial value, while the temperature in the midplane does not increase so much. The vertical outflows are observed from both the upper and lower surfaces, similarly to those seen in the isothermal simulations (Suzuki & Inutsuka 2009; Suzuki et al. 2010).

3.1. Time-averaged Vertical Structures

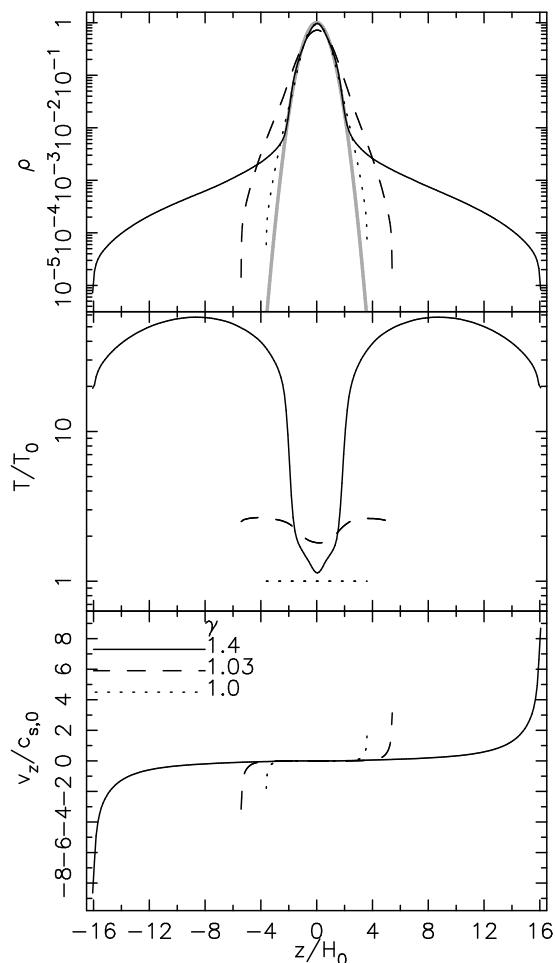


FIG. 3.— Comparison of the horizontally and time averaged vertical structures of the cases with $\gamma = 1.4$ (solid), 1.03 (dashed), and 1.0 (dotted). The horizontal axis is z in unit of the initial H_0 . From the top to the bottom, the densities, the temperatures normalized by the initial values, the vertical velocities normalized by the initial sound speed are compared. The gray thick line in the top panel indicates the initial density profile.

Figure 3 compares the horizontally and time averaged vertical structures on z/H_0 of the three cases with

$\gamma = 1.4$ (solid lines), 1.03 (dashed lines), and 1.0 (dotted lines). Here the time averages are taken over Δt_{ave} in Table 1, after the quasi-steady saturations are achieved (Figure 1). The top panel shows that the gas is lifted up in all the cases compared to the initial profile (gray thick line). In the isothermal ($\gamma = 1.0$) case the gas is lifted up by the magnetic energy as will be discussed in §3.2, which finally connects to the disk winds (Suzuki & Inutsuka 2009; Suzuki et al. 2010). In the non-isothermal cases, the gas is more drastically lifted up. This is because the regions at high altitudes, $|z| \gtrsim 4H_0$, are heated up to form the hot coronae as illustrated in the middle panel and the gas pressure itself supports to lift up the gas, in addition to the magnetic pressure.

The bottom panel of Figure 3 shows that the vertical outflows are accelerated in the surface regions where the densities decrease to $\sim 10^{-4}$ of ρ_{mid} . Since the gas is lifted up to higher altitudes in the cases with larger γ , the onset positions of the disk winds are also located at higher altitudes. By these outflows, the total mass in the simulation box of each case gradually decreases with time. We found that typically 5-10 % of the initial mass is lost until the end of the simulations, 200 rotations.

The existence of the hot coronae above the cool mid-plane region is quite different from some results of recent stratified shearing box simulations. For instance, Bodo et al. (2012) performed the simulations with fixing the temperatures to the initial value ($T = T_0$) and the velocities to zero ($v_z = 0$) at the top and bottom z boundaries. They showed that the maximum temperature is obtained at the midplane and the temperature monotonically decreases to the surfaces. This shows that the boundary condition at the z boundaries play a significant role in the vertical temperature and velocity structures.

In Figure 4, we compare the vertical structures as functions of z in the final scale height, $\int_0^z dz/\langle h(z) \rangle_{\Delta t_{\text{ave}},x,y}$ instead of z/H_0 . The coronal structure of the case with $\gamma = 1.4$ is clearly seen in the first and second panels. The temperature increases drastically around $\int_0^z dz/\langle h(z) \rangle_{\Delta t_{\text{ave}},x,y} \approx \pm 1.5$ to 50 times of T_0 (second panel), and the density decreases across these transition regions to keep the nearly pressure-balanced structure. The third panel shows that the v_z structures resemble each other in these $\int_0^z dz/\langle h(z) \rangle_{\Delta t_{\text{ave}},x,y} - v_z/c_{s,0}$ plots, in contrast to the $z/H_0 - v_z/c_{s,0}$ plots in Figure 3.

The bottom panel displays the plasma β values, $\langle\beta\rangle_{\Delta t_{\text{ave}},x,y} = 8\pi\langle p\rangle_{\Delta t_{\text{ave}},x,y}/\langle B^2\rangle_{\Delta t_{\text{ave}},x,y}$ (left axis), and the α values, $\langle\alpha\rangle_{\Delta t_{\text{ave}},x,y} = \langle\rho v_x \delta v_y - B_x B_y/4\pi\rangle_{\Delta t_{\text{ave}},x,y}/\langle p\rangle_{\Delta t_{\text{ave}},x,y}$ (right axis). $\langle\beta\rangle_{\Delta t_{\text{ave}},x,y}$ is larger for smaller γ mainly because the gas pressure is systematically larger by the heating. Accordingly, $\langle\alpha\rangle_{\Delta t_{\text{ave}},x,y}$ is smaller for larger γ . We should note that the large β and small α values around the midplane in the case with $\gamma = 1.4$ are partly because of the insufficient resolution. In this case, the initial scale height, H_0 , is resolved by 8 mesh points. Although one scale height, $h(z)$, is eventually resolved by a larger number of grids, $\sim 10 - 15$, it is still insufficient to capture fine turbulent structure by the MRI (Simon et al. 2009; Hawley et al. 2011, 2013). Therefore, the magnetic fields might not be well developed to the physically saturated state in this case, giving the larger β and the smaller α .

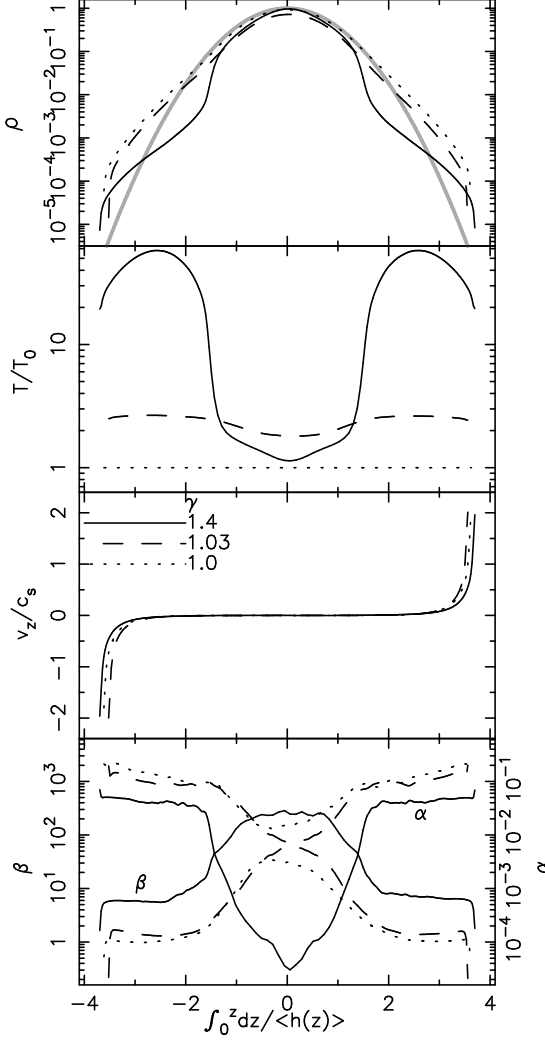


FIG. 4.— Comparison of the horizontally and time averaged vertical structures of the cases with $\gamma = 1.4$ (solid), 1.03 (dashed), and 1.0 (dotted). The horizontal axis, $\int_0^z dz/\langle h(z) \rangle$, is measured in the final scale heights after heated up instead of z/H_0 . The upper three panels show the same quantities as in Figure 3 but in the third panel v_z are normalized by the final sound speeds averaged over Δt_{ave} after the saturations. The bottom panel shows the plasma β values (left axis) and the α values (right axis).

3.2. Driving Vertical Outflows

Not only the three cases in Figures 3 and 4 but also the other all cases with different γ exhibit the vertical outflows. We inspect how the driving mechanism of these disk winds is different for different γ . By rearranging Equation (1), we can derive an Eulerian form of the energy equation

$$\begin{aligned}
 & \frac{\partial}{\partial t} \left[\rho \frac{v^2}{2} + \rho e + \frac{B^2}{8\pi} + \rho \Psi \right] \\
 &= -\nabla \cdot \left[\rho \mathbf{v} \left(\frac{v^2}{2} + h + \Psi \right) - \frac{1}{4\pi} (\mathbf{v} \times \mathbf{B}) \times \mathbf{B} \right] \\
 &= -\nabla \cdot \left[\left\{ \mathbf{v} \left(\rho \frac{v^2}{2} + \rho e + \frac{B^2}{8\pi} + \rho \Psi \right) \right\} \right. \\
 & \quad \left. + \left\{ \left(p + \frac{B^2}{8\pi} \right) \mathbf{v} - \frac{\mathbf{B}}{4\pi} (\mathbf{B} \cdot \mathbf{v}) \right\} \right], \quad (8)
 \end{aligned}$$

where $\Psi \equiv \frac{\Omega^2}{2}(z^2 - 3x^2)$ and $h = e + p/\rho$. One can see from the last equality, the energy flux can be divided into the two parts; the first $\{ \}$ bracket indicates the energy advected with \mathbf{v} and the second $\{ \}$ bracket indicates the work acting on gas, which appears in the spatial derivative term in the Lagrangian form (Equation 1). Here, we examine this work component in the simulations. The z component of these terms can be explicitly written as

$$\begin{aligned}
 & \left(p + \frac{B^2}{8\pi} \right) v - \frac{\mathbf{B}}{4\pi} (\mathbf{B} \cdot \mathbf{v}) \\
 &= p v_z + \frac{B_{\perp}^2}{8\pi} v_z - \frac{B_z}{4\pi} B_{\perp} v_{\perp} - \frac{B_z^2}{8\pi} v_z, \quad (9)
 \end{aligned}$$

where $B_{\perp}^2 = B_x^2 + B_y^2$ and $B_{\perp} v_{\perp} = B_x v_x + B_y v_y$. The first, second, and third terms indicate the work by gas pressure, magnetic pressure, and magnetic tension, respectively. The last term is canceled out by a term from the advection component. We compare the first – third terms of the three cases with $\gamma = 1.4$ (left panel), 1.03 (middle panel), and 1.0 (right panel) in Figure 5.

If a line in Figure 5 decreases with increasing z in the $z > 0$ region, the force acts on gas to drive a vertical upflow, and vice versa in the $z < 0$ region. In the isothermal ($\gamma = 1.0$) case, the magnetic pressure (dotted line) and tension (solid line) comparably contribute to driving the vertical outflows, while the contribution from the gas pressure is quite small. The “injection regions” of the magnetic tension form around $\int_0^z dz/\langle h(z) \rangle_{\Delta t_{\text{ave}}, x, y} \approx \pm 1.5$ as pointed out by Suzuki & Inutsuka (2009); from these regions, the Poynting fluxes associated with the tension are injecting toward both the midplane and surface directions.

On the other hand, in the case with $\gamma = 1.4$, the gas pressure largely dominates the magnetic components in driving the disk winds. In this case, the magnetic energy in low-altitude regions once dissipates to heat up the gas. The gas pressure, which increases owing to the magnetic heating, finally contributes to driving the vertical outflows. This is in contrast to the isothermal case, in which the magnetic fields directly drive the vertical outflows by the magnetic pressure and tension. The behaviors of the case with $\gamma = 1.03$ lie between the two cases. While the largest contribution is from the magnetic pressure, the magnetic tension and the gas pressure also play a significant role.

Inspecting all the cases with different γ , we can conclude the following results on the driving mechanisms of the disk winds: While in the isothermal and small $\gamma \lesssim 1.03$ cases the vertical outflows are mainly driven by the Poynting flux, in the large $\gamma \gtrsim 1.1$ cases, the gas pressure dominantly drives the vertical outflows. However, we should note that, even in the large γ cases the magnetic fields play an important role, because the gas pressure is maintained by the dissipation of the magnetic energy which is amplified by the MRI.

The difference of the driving mechanisms influences the time-dependency of the disk winds. Figure 6 compares the $t - z$ diagrams of the mass flux of the cases with $\gamma = 1.4$ (upper panel) and 1.0 (lower panel). The two cases show quite different appearances. The isothermal case (lower panel) shows a clearer on-off nature of the disk winds. As reported in Suzuki & Inutsuka (2009),

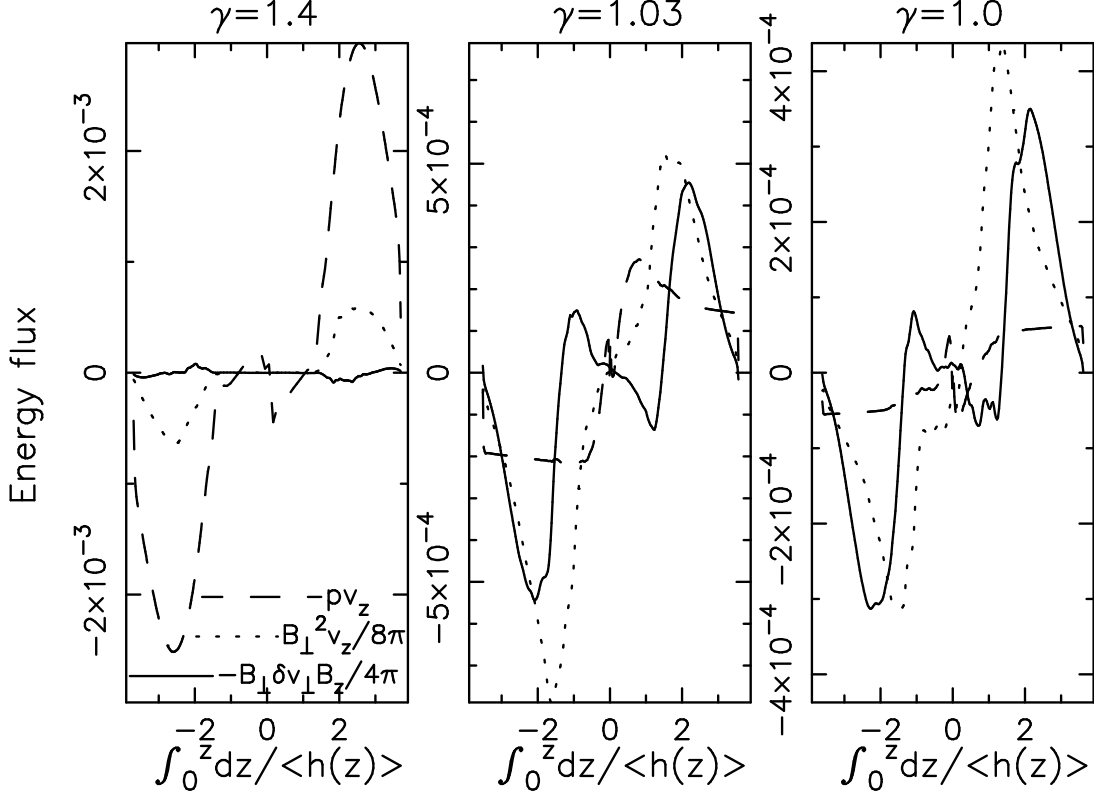


FIG. 5.— Comparison of the horizontally and time averaged vertical structures of the gas pressure (*dashed*), the magnetic pressure (*dotted*), and the magnetic tension (*solid*) terms of the cases with $\gamma = 1.4$ (left), 1.03 (middle), and 1.0 (right). See *text* (Equations 8 & 9 and their explanations) for details.

it is related to the quasi-periodic breakup of channel-mode flows with 5-10 rotation times. On the other hand, the case with $\gamma = 1.4$ exhibits smoother structure in the coronal regions, $|z| > 2H_0$, with rather quasi-steady vertical outflows. The midplane region ($|z| < 2H_0$) with $T/T_0 < 10$ (Figures 3 & 4) seems to be separated to the coronal regions by the transition regions at $|z| \approx 2H_0$. The quasi-steady nature of the disk winds in this case is related to the fact that the vertical outflows are mainly driven by the gas pressure. The coronal temperatures are more or less uniformly distributed in $|z| \approx 2H_0$, and the force by the gas pressure gradient are more time-steady, which is in contrast to the strong intermittency of the Poynting flux-driven outflows in the isothermal case.

3.3. Time & Spatial Averaged Quantities with γ

We summarize typical time-averaged quantities of the simulations with different γ . The top panel of Figure 7 shows the dependence of the mass flux of the disk winds. The shown quantity is

$$\langle C_w \rangle_{\Delta t_{ave}, x, y} = [\langle (\rho v_z)_{top} \rangle + \langle (-\rho v_z)_{bot} \rangle] / \langle (\rho c_s)_{mid} \rangle, \quad (10)$$

where the subscripts, ‘top’ and ‘bot’, indicates the top and bottom boundaries of the simulation box, and the subscript ‘mid’ stands for the midplane. The variables in the brackets on the right hand side are also horizontally and time averaged. The meaning of Equation (10) would be clear, the sum of the mass fluxes from the upper and lower simulation boundaries, which is further normalized by the horizontally and time averaged ρc_s at

the midplane. Note that the $-$ sign for the mass flux from the bottom surface is to pick up the outflowing direction.

The data points show that the nondimensional mass flux, C_w , seems to be almost independent from γ and is distributed within a factor of 2; C_w dose not depend on the main driving mechanism of the vertical outflows, either Poynting flux-driven (smaller γ) or gas pressure-driven (larger γ), which is a little surprising. We suppose that the main reason of the insensitive C_w to γ is that the original source of the vertical outflows is the magnetic energy. The magnetic energy becomes relatively important with an elevating altitude from the midplane with decreasing density, and at the locations with $\rho \approx 10^{-4} \rho_{mid}$ the magnetic energy starts to be gradually converted to other forms, which is almost independent from γ . In the small γ regime the magnetic pressure and tension directly accelerate the Poynting flux-driven vertical outflows, while in the large γ regime the magnetic energy is firstly transferred to the internal energy, the coronal heating in other words, and then the disk winds are driven by the gas pressure of the hot coronae. The locations (at $\rho \approx 10^{-4} \rho_{mid}$) of the energy conversion regulate the final mass flux, $C_w \approx 2 \times 10^{-4}$, which is insensitive to γ .

The relative comparison of C_w among different γ cases of the simulations is meaningful since the vertical box sizes are tuned to give 7.1–7.4 in units of the final scale heights (Table 1). However, we should cautiously note that the absolute values of C_w should be taken with cares

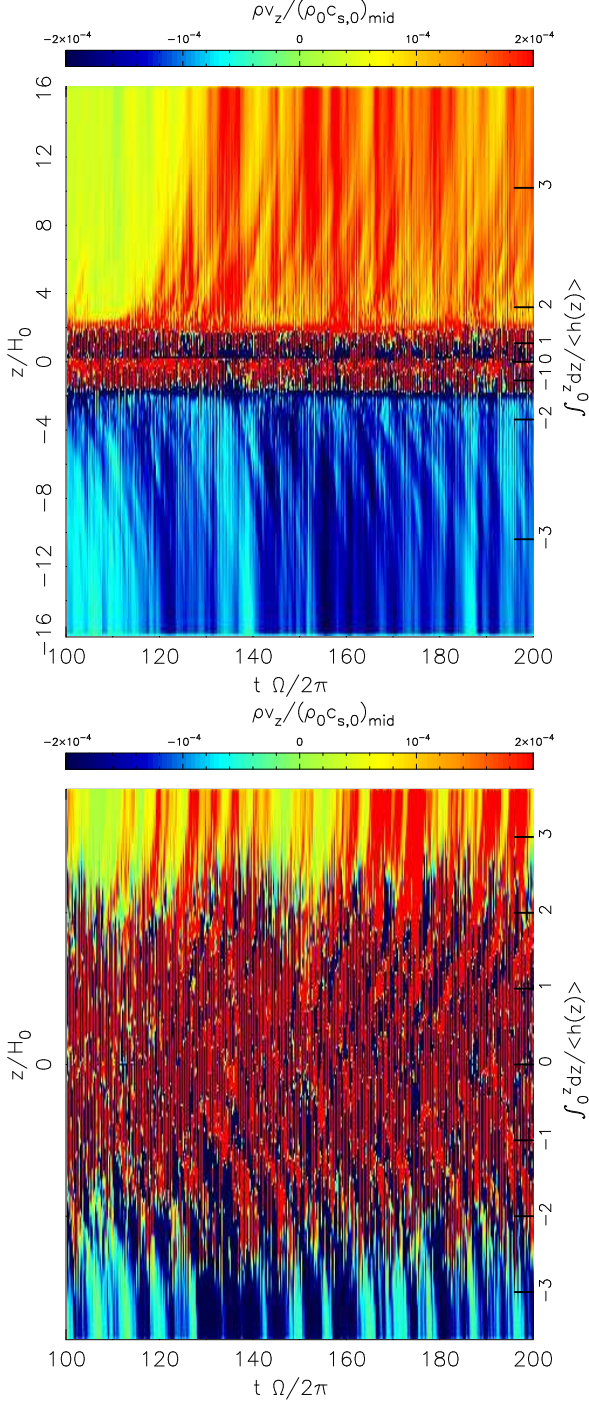


FIG. 6.— Time-distance diagrams of the normalized mass flux, $\rho v_z / (\rho_0 c_{s,0})_{\text{mid}}$ of the cases with $\gamma = 1.4$ (upper) and 1.0 (lower). The horizontal axis ($t\Omega/2\pi$) denotes time in units of rotation. The vertical axis shows z ; on the right shown in distance in units of the initial scale height, z/H_0 , and on the left shown is distance in units of the final scale height, $\int_0^z dz / \langle h(z) \rangle_{\Delta t_{\text{ave}}, x, y}$.

because they depend on the vertical box sizes (Suzuki et al. 2010; Fromang et al. 2013); a larger vertical box would give a smaller C_W .

The middle panel of Figure 7 presents the box- and time-averaged $\langle \alpha \rangle_{\Delta t_{\text{ave}}, x, y, z}$ values. We do not find any monotonic trend of $\langle \alpha \rangle_{\Delta t_{\text{ave}}, x, y, z}$ with γ and the values are typically $(1-3) \times 10^{-2}$. However, we cannot proceed

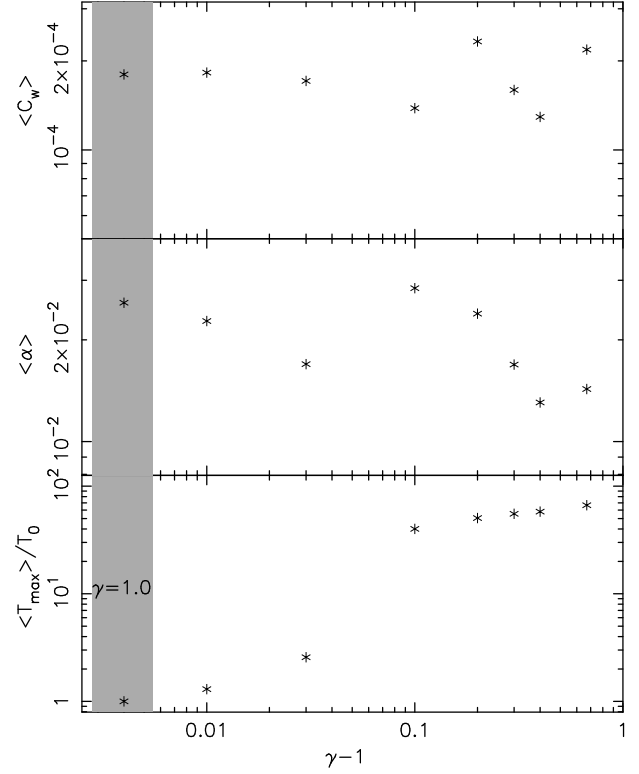


FIG. 7.— Dependences of time averaged three quantities on $\gamma-1$. Shown are the sum of the nondimensionalized mass fluxes of the vertical outflows, $\langle C_w \rangle_{\Delta t_{\text{ave}}, x, y}$, from the upper and lower surfaces (eq.10; *top*), the peak temperature, $\langle T_{\text{max}} \rangle_{\Delta t_{\text{ave}}, x, y}$ (*middle*), and the sum of the box-averaged Maxwell and Reynolds stresses, $\langle \alpha \rangle_{\Delta t_{\text{ave}}, x, y, z}$, (*bottom*). In the shaded region at the left most location the results of the isothermal case ($\gamma = 1.0$) are plotted.

detailed saturation arguments (e.g. Simon et al. 2009; Hawley et al. 2011), since the resolution of the simulations is low and the box size is not large enough.

The bottom panel of Figure 7 compares the maximum temperatures, T_{max} , normalized by the initial value, T_0 , of the different γ cases. T_{max} is derived from the horizontally and time averaged vertical structure; temperature is locally higher than T_{max} at some instances. One can see a clear increasing trend with γ , because larger γ simply corresponds to smaller net cooling (cooling - heating). Moreover, T_{max}/T_0 jumps up from $\gamma = 1.01$ to $\gamma = 1.1$, which corresponds to the change of the regime from the Poynting flux-driven winds to the gas pressure-driven winds.

3.4. Wave Phenomena

In Suzuki & Inutsuka (2009) we examined the vertical energy flux associated with wave-like activities and found Alfvénic and sound-like waves propagating to both upward and downward directions. Following the procedure in Suzuki & Inutsuka (2009), we inspect the vertical structures of two quantities, $-B_z \delta v_{\perp} B_{\perp} / 4\pi$ and $\delta \rho \delta v_z \gamma c_s^2$. $-B_z \delta v_{\perp} B_{\perp} / 4\pi$ is the Poynting flux of magnetic tension, as discussed in Equation (8), and can be rewritten as

$$-\frac{1}{4\pi} B_z \delta v_{\perp} B_{\perp} = \rho v_{A,z} (\delta v_{\perp,+}^2 - \delta v_{\perp,-}^2), \quad (11)$$

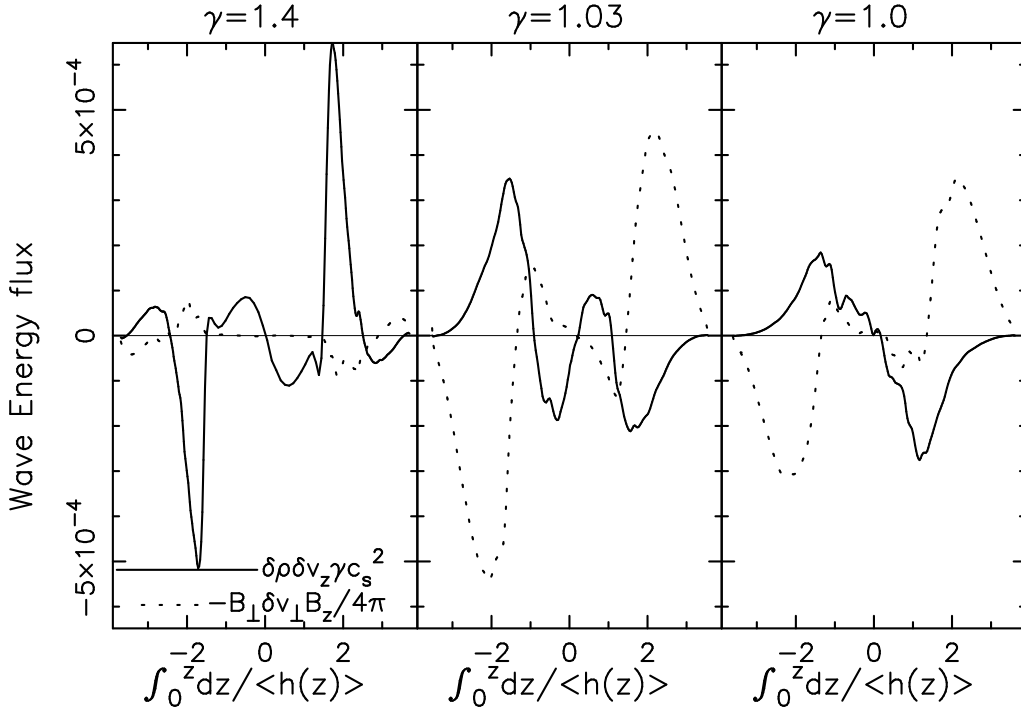


FIG. 8.— Comparison of the horizontally and time averaged vertical structures of $-B_z \delta v_\perp B_\perp / 4\pi$ (dotted) and $\delta \rho \delta v_z \gamma c_s^2$ (solid) for the cases with $\gamma = 1.4$ (left), 1.03 (middle), and 1.0 (right). They correspond to the net energy fluxes associated with Alfvénic and sound-like waves, respectively. See text (Equations 11 & 12 and their explanations) for details.

where $v_{A,z} = B_z / \sqrt{4\pi\rho}$ is Alfvén speed along the z direction, and $\delta v_{\perp,\pm} = \frac{1}{2}(\delta v_\perp \mp B_\perp / \sqrt{4\pi\rho})$ are Elsässer variables, which correspond to the amplitudes of Alfvén waves propagating to the $\pm z$ -directions. Thus, $-B_z \delta v_\perp B_\perp / 4\pi$ corresponds to the net Poynting flux associated with propagating Alfvénic disturbances to the $+z$ direction. $\delta \rho \delta v_z \gamma c_s^2$ is also rewritten as

$$\delta \rho \delta v_z \gamma c_s^2 = \rho \sqrt{\gamma} c_s (\delta v_{\parallel,+}^2 - \delta v_{\parallel,-}^2), \quad (12)$$

where $\delta v_{\parallel,\pm} = \frac{1}{2}(\delta v_z \pm \sqrt{\gamma} c_s \frac{\delta \rho}{\rho})$ denote the amplitudes of sound waves³ propagating to the $\pm z$ -directions. Here, note that the sound speed is expressed as $\sqrt{\gamma} c_s$ since in this paper we define c_s as isothermal sound speed.

Figure 8 compares these quantities of the three cases with $\gamma = 1.4$ (left panel), 1.03 (middle panel), and 1.0 (right panel). As already discussed in Suzuki & Inutsuka (2009), in the isothermal case sound-like waves propagating to the midplane are observed. The peak values are located at the injection regions, $\int_0^z dz / \langle h(z) \rangle_{\Delta t_{ave,x,y}} \approx \pm 1.5$ for the Alfvénic waves (dotted line); Alfvénic waves are injected from these regions mostly associated with the breakup of channel flows.

The case with $\gamma = 1.03$ exhibits the similar structures except for $\delta \rho \delta v_z \gamma c_s^2$ (solid line) in the midplane region, $|\int_0^z dz / \langle h(z) \rangle_{\Delta t_{ave,x,y}}| < 1$; the direction of the sound-like waves is upward (to both $\pm z$) from the midplane, which is opposite to that in the isothermal case.

³ Strictly speaking, these are magnetosonic waves, namely the fast mode in the high β plasma, and the slow mode that propagates along z in the low β plasma. Note also that the signs are opposite for $\delta v_{\perp,\pm}$ and $\delta v_{\parallel,\pm}$, reflecting the transverse and longitudinal characters.

The case with $\gamma = 1.4$ shows very different behaviors. The energy flux of Alfvénic waves is mostly dominated by that of sound-like waves. In particular, it is nearly zero in the midplane region between the transition regions at $\int_0^z dz / \langle h(z) \rangle_{\Delta t_{ave,x,y}} \approx \pm 1.5$, which separate the cool midplane from the above hot coronae. The midplane region is protected from the magnetic perturbations in the upper coronae because the Alfvénic disturbances are reflected at the transition regions (see §3.5). The direction of the sound-like waves in this region is to the midplane. The large jumps are also seen in the sound-like waves at the transition regions; the sound speed also changes abruptly there owing to the change of the temperature, which causes the reflection of sound-like waves. Thus, the sound-like waves are confined in the cool midplane region.

Sound waves are associated with density perturbations. Therefore, we expect that the different structures of $\delta \rho \delta v_z \gamma c_s^2$ will give different density perturbations. In Figure 9 we compare the vertical structures of the nondimensional density perturbations, which are calculated as

$$\langle \frac{\delta \rho}{\rho} \rangle_{\Delta t_{ave,x,y}} = \frac{\langle \sqrt{(\rho - \langle \rho \rangle_{x,y})^2} \rangle_{\Delta t_{ave,x,y}}}{\langle \rho \rangle_{\Delta t_{ave,x,y}}}. \quad (13)$$

The cases with $\gamma = 1.03$ (dashed line) and 1.0 (dotted line) exhibit similar vertical structures; larger $\delta \rho / \rho \approx 0.5$ in the surface regions decrease to ~ 0.05 at the midplane. On the other hand, the case with $\gamma = 1.4$ shows complicated structure. The jumps at $\int_0^z dz / \langle h(z) \rangle_{\Delta t_{ave,x,y}} \approx \pm 1.5$ coincide with the transition regions between the upper hot coronae and the lower cool midplane. In the midplane region, $\delta \rho / \rho \approx 0.1$ is larger than those obtained in the other two cases, probably because of the confinement

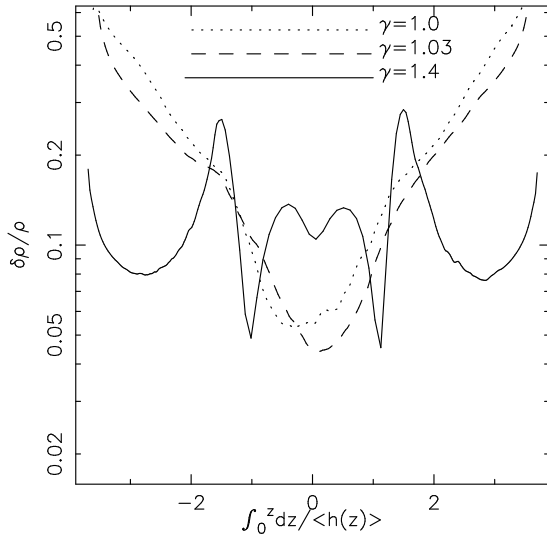


FIG. 9.— Comparison of the horizontally and time averaged nondimensional density fluctuations, $\delta\rho/\rho$, of cases with $\gamma = 1.4$ (solid), 1.03 (dashed), and 1.0 (dotted).

of the sound-like waves in the midplane region (Figure 8). However in the coronal regions $\delta\rho/\rho \lesssim 0.2$ is much smaller than those in the other cases.

3.5. Toroidal B

The evolution of toroidal magnetic fields, B_y , is widely discussed in terms of “dynamo” activities in disks by MRI (Brandenburg et al. 1995; Nishikori et al. 2006; Shi et al. 2010). In Figure 10, we compare the $t - z$ diagrams of the cases with $\gamma = 1.4$ (upper panel) and 1.0 (lower panel). The isothermal case (lower panel) exhibits usual quasi-periodic changing of the sign of B_y , as seen by previous works (e.g. Davis et al. 2010). The case with $\gamma = 1.4$ also shows quasi-periodic oscillations of the B_y , but the period is shorter than that in the isothermal case and the amplitude (contrast between red and blue regions) is smaller. This indicates that the toroidal magnetic fields change the sign before the magnetic fields are amplified to the level as strong as that obtained in the isothermal case. This is probably because in the large γ case the magnetic fields are more subject to the gas motion because of the high β condition (Figure 4).

The difference of the time-dependencies is consistent with the time evolutions of $\langle \alpha \rangle_{x,y,z}$ as shown in Figure 1. For larger γ , $\langle \alpha \rangle_{x,y,z}$ shows smaller fluctuations with time, because the dynamics are largely controlled by the gas pressures, which distribute more uniformly in a more time-steady manner, rather than by the magnetic fields, which intermittently pile up associated with channel flows.

Another interesting feature of the nonisothermal case with $\gamma = 1.4$ is that the butterfly pattern triggered in the coronal regions is very vague in the midplane region. The left panel of Figure 5 also shows that the Poynting flux is negligibly small in this region. They imply that the midplane region seems to be protected from the magnetic perturbations in the coronal regions. The transition regions which separate the cool midplane and the hot coronae accompany the large density differences to satisfy the pressure balance structure (Figure 4). This inevitably leads to the large jumps of the Alfvén speed,

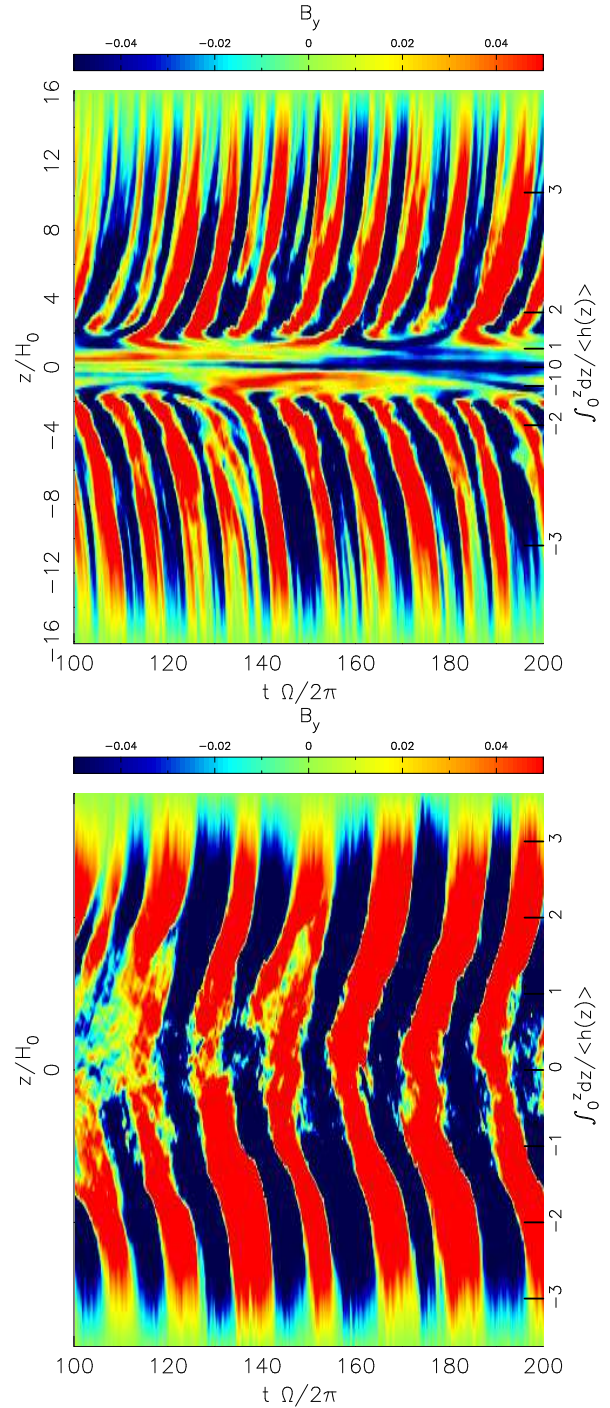


FIG. 10.— Same as Figure 6 but for the toroidal magnetic fields.

$v_{A,z}$, across the transition regions. Then, Alfvénic perturbations arising from magnetic tension suffer reflection and the downward Poynting flux from the coronal regions are mostly reflected back and cannot penetrate the transition regions to the midplane. Reflection of Alfvén waves is widely discussed on the sun because it is very efficient at the transition region between the cool chromosphere and the hot corona (e.g., Suzuki & Inutsuka 2005; Matsumoto & Suzuki 2012). A signature of reflected Alfvén waves is actually observed on the solar surface by the HINODE satellite (Fujimura & Tsuneta

2009). These are quite similar to what we observe in the present simulations with relatively large γ .

4. SUMMARY AND DISCUSSIONS

Using the 3D MHD simulations in the local stratified shearing boxes with weak net vertical magnetic fields, we have studied the formation of the hot coronae and the disk winds induced by the MRI turbulence in the accretion disks. Taking into account the effect of the cooling phenomenologically with the effective ratio of the specific heats, γ , we have inspected how the basic properties are affected by the cooling. Since the simulations are performed in the nondimensional form without any physical scale, the simulations are applicable to various objects. The amplifications of the magnetic fields are observed in all the simulation runs with different γ from 1 to 5/3, which give the time- and box-averaged $\alpha \approx (1-3) \times 10^{-2}$. In terms of the properties of the coronae and the disk winds, we have found that the results are classified into the two regimes.

In the small $\gamma (< 1.03)$ regime, the temperatures in the surface regions are not high because the effect of the heating is weak owing to the small γ . The vertical outflows are directly driven by the Poynting flux associated with the amplified turbulent magnetic fields, they are more time-dependent, involved with the intermittent breakup of large-scale channel flows.

In the large $\gamma (\geq 1.1)$ regime, the hot coronae form by the dissipation of the magnetic energy and the temperatures are ~ 50 times of the initial values with the peak temperature slowly increasing with γ . The vertical outflows are mainly driven by the gas pressure of the hot coronae. Because the spatial distribution of the gas pressure is more uniform than that of the magnetic energy, the disk winds stream out in a more time-steady manner than in the small γ regime. The hot coronae are connected to the cool midplane through the sharp transition regions. Across the transition regions, both the sound and Alfvén speeds change abruptly because of the

jumps of the temperature and the density. The transition regions work as the walls against wave activities. Sound-like waves are confined in the cool midplane region with giving the larger amplitude of the density perturbations. The midplane region is also protected from the magnetic perturbations in the upper coronae.

Although the driving mechanisms and the time-dependencies of the vertical outflows are different for the small and large γ regimes, the time-averaged nondimensional mass fluxes, C_W , are similar each other. This is because in the both regimes the origin that drives the vertical outflows is the magnetic energy that is amplified by the MRI. The magnetic energy is gradually converted at the locations with $\rho \approx 10^{-4} \rho_{\text{mid}}$, directly to the kinetic energies of the disk winds in the small γ regime, or firstly to the thermal energies of the hot coronae that is finally transferred to the disk winds in the large γ regime. The locations of the energy conversions, which are insensitive to γ , control the final C_W . We should cautiously note that the derived mass flux, $C_W \approx 2 \times 10^{-4}$, depends on the vertical box size (Suzuki et al. 2010; Fromang et al. 2013), although the comparisons of different cases with the same vertical box size make sense.

Our treatment of spatially uniform γ is too much simplified. In reality, γ should be non-uniform. Deeper regions near the midplane tend to be more optically thick, which gives larger γ , while in surface regions γ is smaller. In more elaborated models with applications to specific objects, adequate cooling and heating processes should be included with radiative transfer (e.g., Hirose et al. 2006).

The authors thank Prof. Shu-ichiro Inutsuka for many fruitful discussions. This work was supported in part by Grants-in-Aid for Scientific Research from the MEXT of Japan, 22864006. Numerical simulations in this work were carried out with SR16000 at the Yukawa Institute Computer Facility and with the Cray XT4 and XC30 operated in CfCA, National Astrophysical Observatory of Japan.

REFERENCES

- Bai, X.-N., & Stone, J. M. 2013, *ApJ*, 767, 30
 Balbus, S. A., & Hawley, J. F. 1991, *ApJ*, 376, 214
 —. 1998, *Reviews of Modern Physics*, 70, 1
 Blandford, R. D., & Payne, D. G. 1982, *MNRAS*, 199, 883
 Bodo, G., Cattaneo, F., Mignone, A., & Rossi, P. 2012, *ApJ*, 761, 116
 Brandenburg, A., Nordlund, A., Stein, R. F., & Torkelsson, U. 1995, *ApJ*, 446, 741
 Chandrasekhar, S. 1960, *Proceedings of the National Academy of Science*, 46, 253
 Clarke, D. A. 1996, *ApJ*, 457, 291
 Coffey, D., Bacciotti, F., Woitas, J., Ray, T. P., & Eisloffel, J. 2004, *ApJ*, 604, 758
 Davis, S. W., Stone, J. M., & Pessah, M. E. 2010, *ApJ*, 713, 52
 Flock, M., Dzyurkevich, N., Klahr, H., Turner, N. J., & Henning, T. 2011, *ApJ*, 735, 122
 Fromang, S., Latter, H., Lesur, G., & Ogilvie, G. I. 2013, *A&A*, 552, A71
 Fujimura, D., & Tsuneta, S. 2009, *ApJ*, 702, 1443
 Goldreich, P., & Lynden-Bell, D. 1965, *MNRAS*, 130, 125
 Guan, X., Gammie, C. F., Simon, J. B., & Johnson, B. M. 2009, *ApJ*, 694, 1010
 Hawley, J. F., Gammie, C. F., & Balbus, S. A. 1995, *ApJ*, 440, 742
 Hawley, J. F., Guan, X., & Krolik, J. H. 2011, *ApJ*, 738, 84
 Hawley, J. F., Richers, S. A., Guan, X., & Krolik, J. H. 2013, *ApJ*, 772, 102
 Hirose, S., Krolik, J. H., & Stone, J. M. 2006, *ApJ*, 640, 901
 Hirose, S., & Turner, N. J. 2011, *ApJ*, 732, L30
 Lesur, G., Ferreira, J., & Ogilvie, G. I. 2013, *A&A*, 550, A61
 Lynden-Bell, D., & Pringle, J. E. 1974, *MNRAS*, 168, 603
 Matsumoto, R., & Tajima, T. 1995, *ApJ*, 445, 767
 Matsumoto, T., & Suzuki, T. K. 2012, *ApJ*, 749, 8
 Miller, K. A., & Stone, J. M. 2000, *ApJ*, 534, 398
 Nishikori, H., Machida, M., & Matsumoto, R. 2006, *ApJ*, 641, 862
 Ohashi, N., Hayashi, M., Ho, P. T. P., & Momose, M. 1997, *ApJ*, 475, 211
 Okuzumi, S., & Hirose, S. 2011, *ApJ*, 742, 65
 Pudritz, R. E., & Norman, C. A. 1983, *ApJ*, 274, 677
 Sai, K., Katoh, Y., Terada, N., & Ono, T. 2013, *ApJ*, 767, 165
 Sano, T., Inutsuka, S., & Miyama, S. M. 1999, in *Astrophysics and Space Science Library*, Vol. 240, Numerical Astrophysics, ed. S. M. Miyama, K. Tomisaka, & T. Hanawa, 383
 Sano, T., Inutsuka, S.-i., Turner, N. J., & Stone, J. M. 2004, *ApJ*, 605, 321
 Shakura, N. I., & Sunyaev, R. A. 1973, *A&A*, 24, 337
 Shi, J., Krolik, J. H., & Hirose, S. 2010, *ApJ*, 708, 1716
 Simon, J. B., Hawley, J. F., & Beckwith, K. 2009, *ApJ*, 690, 974
 Stone, J. M., Hawley, J. F., Gammie, C. F., & Balbus, S. A. 1996, *ApJ*, 463, 656
 Suzuki, T. K., & Inutsuka, S.-i. 2005, *ApJ*, 632, L49
 —. 2006, *Journal of Geophysical Research (Space Physics)*, 111, 6101
 —. 2009, *ApJ*, 691, L49
 —. 2013, to be submitted to *ApJ*
 Suzuki, T. K., Muto, T., & Inutsuka, S.-i. 2010, *ApJ*, 718, 1289
 Tombesi, F., Sambruna, R. M., Reeves, J. N., et al. 2010, *ApJ*, 719, 700
 Velikhov, E. P. 1959, *Zh. Eksp. Teor. Fiz.*, 36, 1398